NeuroImage 118 (2015) 49–62

Contents lists available at ScienceDirect

NeuroImage

journal homepage: www.elsevier.com/locate/ynimg

4D MEMRI atlas of neonatal FVB/N mouse brain development

Kamila U. Szulc [a,b], Jason P. Lerch [f,g], Brian J. Nieman [f,g,h], Benjamin B. Bartelle [a,c], Miriam Friedel [f], Giselle A. Suero-Abreu [a,b], Charles Watson [i], Alexandra L. Joyner [j], Daniel H. Turnbull [a,b,c,d,e,*]

[a] Skirball Institute of Biomolecular Medicine, New York University School of Medicine, New York, NY, USA
[b] Biomedical Imaging, New York University School of Medicine, New York, NY, USA
[c] Molecular Biophysics Graduate Programs, New York University School of Medicine, New York, NY, USA
[d] Department of Radiology, New York University School of Medicine, New York, NY, USA
[e] Department of Pathology, New York University School of Medicine, New York, NY, USA
[f] Mouse Imaging Centre, Hospital for Sick Children, Toronto, ON, Canada
[g] Department of Medical Biophysics, University of Toronto, Toronto, ON, Canada
[h] Ontario Institute for Cancer Research, Toronto, ON, Canada
[i] Health Sciences, Curtin University, Perth, Western Australia, Australia
[j] Developmental Biology Program, Sloan-Kettering Institute, New York, NY, USA

ARTICLE INFO

Article history:
Received 4 December 2014
Accepted 13 May 2015
Available online 30 May 2015

Keywords:
Brain nuclei
Cerebellum
Image registration
Mn-enhanced MRI

ABSTRACT

The widespread use of the mouse as a model system to study brain development has created the need for non-invasive neuroimaging methods that can be applied to early postnatal mice. The goal of this study was to optimize in vivo three- (3D) and four-dimensional (4D) manganese (Mn)-enhanced MRI (MEMRI) approaches for acquiring and analyzing data from the developing mouse brain. The combination of custom, stage-dependent holders and self-gated (motion-correcting) 3D MRI sequences enabled the acquisition of high-resolution (100-μm isotropic), motion artifact-free brain images with a high level of contrast due to Mn-enhancement of numerous brain regions and nuclei. We acquired high-quality longitudinal brain images from two groups of FVB/N strain mice, six mice per group, each mouse imaged on alternate odd or even days (6 3D MEMRI images at each day) covering the developmental stages between postnatal days 1 to 11. The effects of Mn-exposure, anesthesia and MRI were assessed, showing small but significant transient effects on body weight and brain volume, which recovered with time and did not result in significant morphological differences when compared to controls. Metrics derived from deformation-based morphometry (DBM) were used for quantitative analysis of changes in volume and position of a number of brain regions. The cerebellum, a brain region undergoing significant changes in size and patterning at early postnatal stages, was analyzed in detail to demonstrate the spatio-temporal characterization made possible by this new atlas of mouse brain development. These results show that MEMRI is a powerful tool for quantitative analysis of mouse brain development, with great potential for in vivo phenotype analysis in mouse models of neurodevelopmental diseases.

Introduction

The availability of the complete genomic sequence of the mouse, together with a large array of techniques for engineering mutations in the genome, has led to the widespread acceptance of the mouse as an excellent model system for studies of mammalian brain development and neurodevelopmental disease (Collins et al., 2007; Cryan and Holmes, 2005; Silverman et al., 2010). This has created a need for effective phenotype analysis in the developing mouse brain, from molecular and cellular changes (Sillitoe and Joyner, 2007), to 3D morphological changes (Nieman et al., 2011), and ultimately to changes in behavior (Crawley, 2012; Silverman et al., 2010) associated with defined genetic modifications. Among the neuroimaging methods available for phenotype analysis in mice, MRI offers relatively high spatial resolution over the entire brain, with an acquisition time compatible with most morphological processes (Nieman and Turnbull, 2010; Turnbull and Mori, 2007). As a noninvasive in vivo imaging approach, MRI also allows longitudinal studies of morphological changes in individual mice, an important requirement in mutants that exhibit variable phenotypes during early postnatal brain development (Szulc et al., 2013; Wadghiri et al., 2004).

MRI of the developing mouse brain poses significant challenges, largely due to limitations in signal-to-noise ratio (SNR)—which in turn limits resolution—and tissue contrast. These limitations stem from the fact that the anatomical structures are small and rapidly changing, and the cellular features that provide the most obvious endogenous contrast

* Corresponding author at: Skirball Institute of Biomolecular Medicine, New York University School of Medicine, 540 First Avenue, New York, NY 10016, USA.
E-mail address: daniel.turnbull@med.nyu.edu (D.H. Turnbull).

http://dx.doi.org/10.1016/j.neuroimage.2015.05.029
1053-8119/

for neuroimaging, such as myelination and the segregation of distinct white and gray matter compartments, are absent or immature in the early postnatal brain. Some success in overcoming these challenges has been achieved using "active staining" with gadolinium-based contrast agents to increase SNR and contrast (Johnson et al., 2002a, 2002b), or by using alternate contrast mechanisms as in diffusion tensor imaging, DTI (Mori et al., 2001). With the exception of lower resolution DTI scans, these approaches generally require fixing the brain and often employ very long acquisition times (12 h or more), which precludes in vivo imaging and longitudinal analyses.

MEMRI has emerged as a unique and effective in vivo imaging approach for a variety of anatomical and functional studies in the mouse brain (Boretius and Frahm, 2011; Chan et al., 2014; Inoue et al., 2011; Koretsky and Silva, 2004; Nieman and Turnbull, 2010; Pautler, 2004, 2006; Silva et al., 2004; Watanabe et al., 2010; Yu et al., 2005). In the developing mouse brain, the increased SNR and contrast due to cellular uptake of paramagnetic Mn ions has made it possible to analyze brain sub-regions and perform morphological phenotype analysis from embryonic to early postnatal stages (Deans et al., 2008; Szulc et al., 2013; Wadghiri et al., 2004). These promising results have provided the motivation to further explore the utility of MEMRI for in vivo longitudinal imaging of the neonatal mouse brain, at developmental time points when non-embryonic lethal phenotypes are first manifested and when there is the most need to detect and characterize subtle brain defects as they unfold in mouse mutants.

The overall objective of this study was to further develop and optimize MEMRI for neonatal neuroimaging, and to acquire a comprehensive set of MEMRI images that will serve as a reference for normal postnatal brain development and for comparison to neurodevelopmental defects in mutant and transgenic mouse models. As such, this paper describes the methods for acquiring and analyzing the time-series data in the 4D atlas, and also introduces the types of neuroanatomical information that can be derived from the atlas. The atlas includes quantitative 3D anatomical data at each stage of brain development between postnatal day (P)1 and P11, consisting of longitudinal datasets from 12 individual mice and registered-averaged data from 6 mice at each developmental stage, allowing analysis of growth rates, volume and shape changes of different brain regions. This 4D MEMRI atlas provides a useful resource for studying normal brain development and a baseline for comparison in phenotypic analyses of mutant mice with brain defects. The atlas will also serve as a guide for designing efficient longitudinal MEMRI experiments with optimal choice of developmental stages and the time between imaging sessions, tailored to the brain regions and specific mutant mouse lines being studied.

Materials and methods

Animals

All mice used in this study were maintained under protocols approved by the Institutional Animal Care and Use Committee of New York University School of Medicine. Paramagnetic Mn ions were delivered to the neonates through lactation via maternal intraperitoneal (IP) injection of $MnCl_2$ solution (30 mM solution in isotonic saline) administered 24–29 h (referred to throughout the text as 24 h) prior to each imaging session (Fig. 1). The maternal Mn dose for each injection was 0.4 mmol/kg, equivalent to 50 mg $MnCl_2$ per kg body weight. Since the neonatal Mn dose was dependent on their access to milk, the size of each litter was reduced to 6 or fewer pups within the first 24 h after birth to reduce the variability in Mn intake due to feeding competition. Inbred mice were used to minimize inter-mouse variability in brain size and morphology, and the FVB/N strain was chosen because of its widespread use in generating transgenic lines, and because it has the most complex cerebellar foliation pattern of the commonly used inbred mouse strains (Sillitoe and Joyner, 2007). Two groups (N = 6 per group) of mice (Taconic, Germantown, NY) were selected from 7 different litters (1–2 mice per litter) and imaged longitudinally. Mice in the first group were imaged 6 times, every other day at the "odd-day" stages from postnatal day (P)1 to P11 (where P0 denotes the day of birth). Mice in the second group were imaged 5 times, every other day at the "even-day" stages from P2 to P10. Days P1–P11 were chosen as representative of the most obvious postnatal growth in the cerebellum and other brain regions. To identify the neonates within each litter that were part of this study, permanent ink was used to

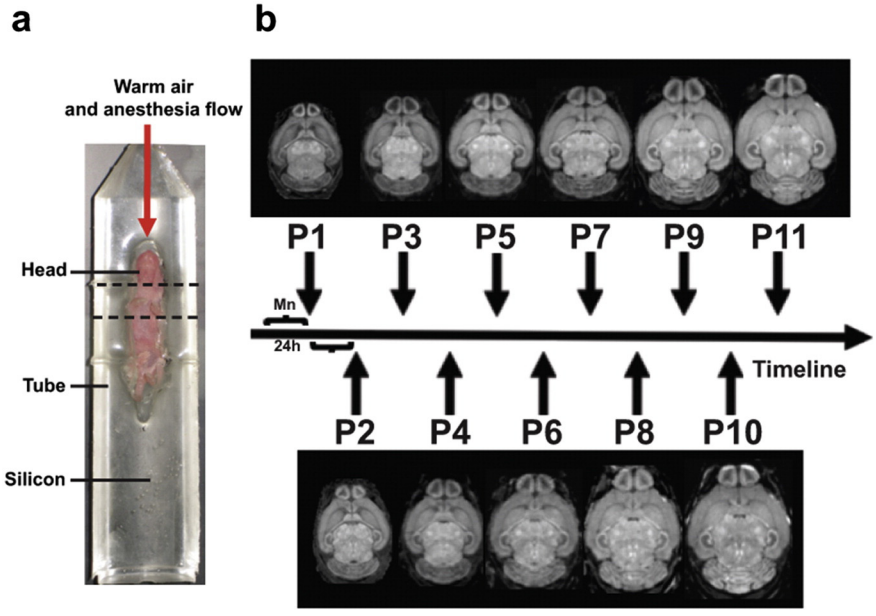

Fig. 1. Longitudinal MEMRI imaging protocol. (a) Custom silicone holders were designed and fabricated in bisected 50-ml plastic tubes for each odd-day stage between P1 and P11 (P3 holder and top view of a mouse pup in supine position are shown) to limit motion and motion-related artifacts during MRI acquisition. Tape was applied to further immobilize the head during imaging (position of tape indicated by the dashed lines). Isoflurane and warm air (red arrow) were directed over the head and body of each pup during imaging. (b) $MnCl_2$ was administered 24-h before each imaging session via maternal IP injection. Each mouse was imaged every other day, on either the odd (P1, P3, P5, P7, P9, P11) or even (P2, P4, P6, P8, P10) days. Example horizontal images are shown from two individual mice, one in the odd group (top panels) and one in the even group (bottom panels).

mark tails during the initial imaging session, and was reapplied daily to avoid fading between sessions.

Body weights were measured in four groups of postnatal mice (G1–G4), housed normally in standard cages with their mothers and littermates from birth (P0) until just before weaning stage at P20. Mice in the experimental group (G1) were exposed to Mn (via maternal injection) every other day from P0 to P10, and imaged with MRI 24-h after each Mn exposure, every other day from P1 to P11. We also included three control groups: i) mice exposed to Mn every other day from P0 to P10 but not anesthetized or imaged with MRI (G2); ii) mice that were exposed to Mn only once at the earliest stage (maternal injection at P0), but not anesthetized or imaged (G3); and iii) mice that were neither exposed to Mn nor anesthetized/imaged with MRI (G4).

To assess the affects of the longitudinal imaging protocol on brain morphology, selected mice from group G1 were also imaged again at P21 after IP injection of $MnCl_2$ at P20. 3D brain images from these mice were compared to mice imaged with MEMRI only once at either P11 or P21, after exposure to $MnCl_2$ at P10 (maternal) or P20 (IP injection), respectively.

Neonatal mouse holders

Custom holders were fabricated to facilitate reproducible positioning at each postnatal stage, with minimal motion during image acquisition (Fig. 1a). To generate the holders, representative mouse pups were selected from a litter every other day from P1 to P11. Each neonatal mouse was euthanized under anesthesia and fixed using cardiac perfusion of phosphate buffered saline (PBS) followed by 4% paraformaldehyde (PFA), positioning the animal in close to a normal supine pose, suitable for scanning, during the fixation process. The fixed bodies were sprayed with food grade silicone mold release (Sprayon S00303) for later extraction, and then coated with 3–5 layers of latex (Amaco) and cured overnight until fully set. After extracting the fixed bodies, the latex negative molds were again lubricated and filled with melted microcrystalline wax (Sculpture House). Once set, the silica wax castings were released from the mold. These silica wax forms, resembling the neonatal mice from which they were modeled, were tough and flexible allowing for minor adjustments to the pose for the final holder. The wax "limbs" were sculpted along the ventral side of the neonate form to provide space for the legs of the living mice in the final holder. For each stage, the final positive form was pinned into place in a 50 ml centrifuge tube (Falcon, BD Biosciences), split in half lengthwise, which fit snugly into the MRI coil. The split 50 ml tubes were capped at the end, filled with a soft casting silicone (Silane, Dow Corning) and allowed to cure overnight. The pins and positive forms were then removed and the finished holders were cleaned before use. Using this procedure a total of six holders were fabricated, modeled on P1, P3, P5, P7, P9 and P11 neonates. In general, each of the holders could be used to image mice $\pm$ 1 day from the stage it was designed for. For example, the P3 holder could also be used to image mice at P2 through P4.

Image acquisition

Images were acquired on a Bruker Biospec imaging system with an Avance II console running Paravision 4 software (Bruker BioSpin MRI, Ettlingen, Germany), interfaced to a 7T 20-cm horizontal bore magnet (Magnex Scientific Ltd., Yarnton, UK). The system utilized actively shielded gradients (BGA9-S, 750 mT/m gradient strength; Bruker) and a 25-mm (ID) quadrature, transmit/receive Litzcage coil (Doty Scientific, Columbia, SC, USA). Three-dimensional (3D) T1-weighted gradient echo images (echo/repetition times, TE/TR = 3.6 ms/50 ms; flip angle = 40°; matrix size = 256 × 256 × 135; number of averages = 2; total acquisition time = 2 h 18 min; isotropic resolution = 100 μm) were acquired using a self-gated sequence to minimize motion artifacts and monitor respiration (Nieman et al., 2009). As described previously, the self-gated sequence was created by modifying a standard 3D gradient-echo sequence. Specifically, a small time delay was introduced between the start of the readout dephase gradient pulse and the two phase-encode pulses to allow signal acquisition during the initial part of the readout dephasing, thus providing low-resolution spatial information in the readout dimension consistent across all TR periods. This extra information was used in the reconstruction process, enabling identification of acquisitions corrupted by motion and subsequent omission from the reconstruction.

During scanning, the neonatal mice were maintained in the custom holders under anesthesia, using 0.5–1% isoflurane in air. To maintain normal body temperatures, warm air was blown over the neonates with the isoflurane (Fig. 1a). Respiratory motion was monitored using the self-gating signal, from which a respiratory trace was derived and displayed in real time on a computer monitor, allowing for adjustments of anesthesia during scanning in order to maintain a stable respiratory rate (30 $\pm$ 5 breaths/min). After imaging, the neonatal mice required 15–20 min for recovery, in a separate cage placed on a heating pad before returning to their mothers and littermates.

Image analysis

Developmental time-series registration

At its core, our approach for analyzing the developmental MEMRI data relies on image registration, where differences between two images (I and J) are captured by the transformation that maps one onto the other. Multiple algorithms have been proposed to optimally perform this alignment (Klein et al., 2009); in this study, we adopted the Lagrangian diffeomorphic registration technique implemented in the ANTs toolkit (Avants et al., 2006, 2008). This registration method uses symmetric normalization (SyN) to create a mapping between images I and J. Briefly, SyN weights the contributions of I and J equally in finding the transformation between them. This transformation is invertible and, if both I and J are deformed to the midpoint of the transform, they will be identical.

The alignment of one image to another must be placed within the larger context of analyzing the full developmental dataset consisting of multiple subjects (n) with repeated image acquisitions (m) for each. There are several registration strategies that can be pursued towards the goal of providing insights into both individual and population level trends. A successful strategy needs to (a) map all m images for any individual subject to determine the evolution in local brain shape over time, and (b) map all n subjects into a common space so that differences within the population at any one point in time as well as in evolution across time can be captured. For the type of data employed in this study, achieving (b) can be a challenge, as not every subject in the data set can be aligned to every other subject (e.g. it is not possible to accurately register a P1 scan to a P11 scan, even for the same mouse).

Our chosen registration strategy relies on *group-wise registrations*, taking advantage of the balanced study design of the data. Briefly, *group-wise registration* proceeds as follows: after rigidly aligning all scans into the same coordinate space with a 6-parameter transform and correcting for non-uniformity artifacts using the N3 algorithm (Sled et al., 1998), each scan is aligned with all other scans in the data set via uniform scales, shears, rotations and translations. From these alignments, the best possible linear average (atlas) of all subjects is created. This atlas provides the starting point for an iterative non-linear registration process; all scans are aligned towards this atlas, resampled with the resulting transforms, and averaged to create a newer, more accurate atlas. This process is repeated three times. Overlapping group-wise registrations are performed on all scans from adjacent days within the *odd day cohort* and *even day cohort* as illustrated in Fig. 2. For example, a group-wise average is created from all P3 and P5 scans, and a separate group-wise average from all P5 and P7 scans. The two cohorts are brought into a common space by a group-wise registration of the P10 and P11 scans.

The ability to analyze each subject's time series is maintained through overlapping adjacent scans. Each scan can be mapped to any

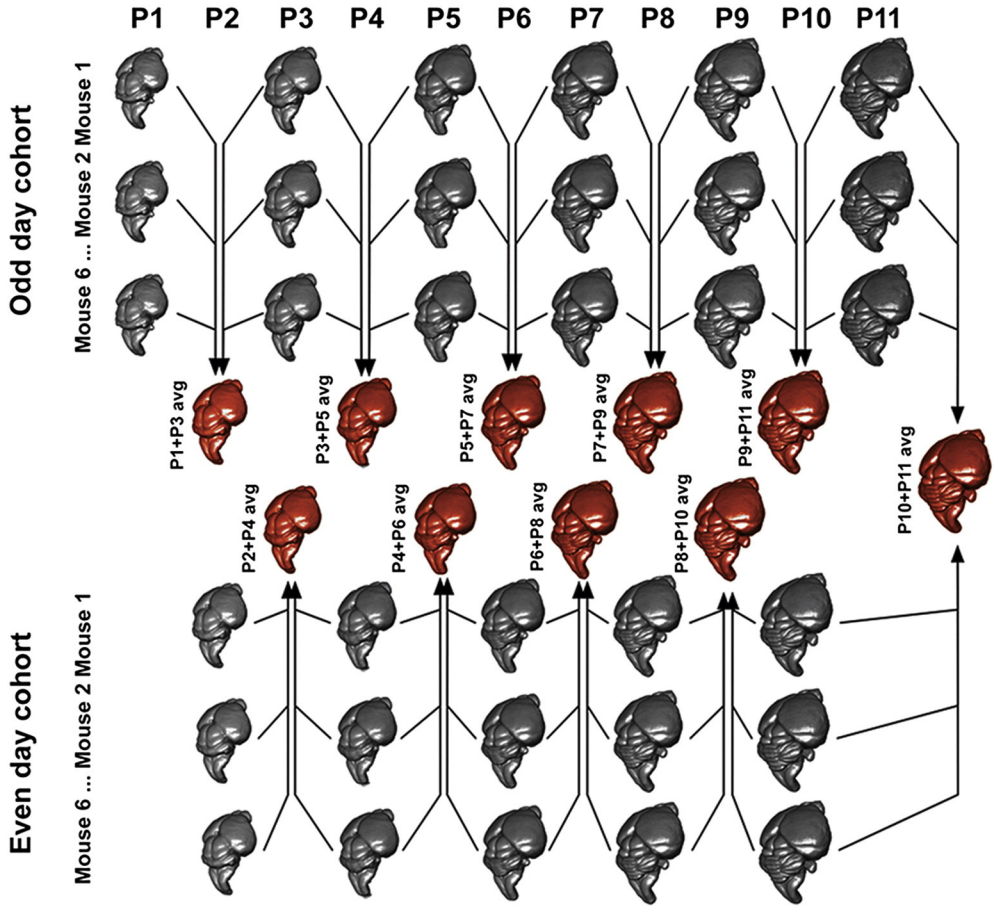

Fig. 2. Longitudinal data analysis through overlapping group-wise registrations. The analysis strategy employed in this study takes advantage of the improved registration performance and numerical stability of group-wise registrations. Adjacent days for each cohort are aligned together, so that every brain, with the exception of those at the beginning of the series, participates in two group-wise registrations. For example, the P5 scans are incorporated in both a registration of all P3 and P5 scans and in another registration of all P5 and P7 scans. The even- and odd-day cohorts are joined by registering the P10 and P11 scans together.

other scan in the series by using appropriate forward and inverse transformations. For example, the following transform concatenations would bring a P7 scan into the common space (P10.5) created by the group-wise registration of all P10 and P11 scans:

$$T_{P7\to P10.5} = T_{P7\to \mathrm{Avg}(P7+P9)} \oplus T_{\mathrm{Avg}(P7+P9)\to P9} \oplus T_{P9\to \mathrm{Avg}(P9+P11)} \oplus T_{\mathrm{Avg}(P9+P11)\to P9} \oplus T_{P11\to P10.5} \quad (1)$$

In Eq. (1) averages are denoted by Avg($Pi + Pj$), so the average from the P9 + P11 group-wise registration is denoted as Avg($P9 + P11$). Transform concatenation is indicated by ⊕. Although we explicitly constructed $T_{P7\to P10.5}$, for much of our analysis we also require $T_{P10.5\to P7}$, which can be attained simply by applying the inverse of the transform constructed in Eq. (1). From these inverted transforms (encoded by displacement fields), we can compute the Jacobian determinant (in P10.5 space) for each transform. This gives a measure of growth or shrinkage at every voxel for every image in the dataset.

The registration algorithms require sufficient homology between scans to work well. To ascertain which post-natal stages can be accurately registered to which other postnatal stages, and thus to understand our accuracy and to inform future study design, we aligned average images from each day to every other day. Accuracy was then computed using a manually segmented P10 + P11 average image and the Kappa statistic:

$$\kappa = \frac{2a}{2a+b+c} \quad (2)$$

where a is common to the automatic segmentation and the ground truth, $b + c$ is the sum of the voxels uniquely identified by the segmentation and the ground truth respectively. κ takes on values between 0 and 1, with 1 indicating perfect agreement and 0 indicating chance agreement (Chakravarty et al., 2013; Cohen, 1960; Collins and Pruessner, 2010; Klein et al., 2009).

Automated time-series analyses for volume and position

Volume analyses were performed on a per voxel basis and also on a 3D region-of-interest basis across all the developmental time points. For the regional analysis, brain structures of interest were outlined on the average P11 image, which was resampled to 25-μm isotropic resolution in Amira (v5.2, Mercury Computer Systems-TGS). Since all the images in the developmental time series (including the P11 images) from both the even and odd cohorts of mice were registered to the average P10 + P11 image, once a region was defined in P11 space it could be mapped to each earlier time point via inverse transforms. This allowed for automated quantification of the volume at each developmental stage. The data was fit using linear mixed-effects model with a third order spline, and 95% confidence levels were calculated. Mixed-effects models incorporate fixed and random effects, allowing modeling of data from the same subject over time and more powerful analysis of longitudinal studies (Pinheiro and Bates, 2000). The same modeling approach was also employed to track the position of points placed at the base and tip of selected cerebellar folia, mapping through the registrations to determine the displacements of these points during development.

The general formula for a linear mixed effects model is as follows (Laird and Ware, 1982):

$$y_{ij} = \beta_1 x_{1ij} + \cdots + \beta_p x_{pij} + b_{i1} z_{1ij} + \cdots + b_{iq} z_{qij} + \varepsilon_{ij} \quad (3)$$

In Eq. (3), y_{ij} is a response variable for the jth measurement in the ith subject. For the purposes of this study, y_{ij} is a measurement in mouse i on the jth day. These measurements correspond to either the value of the Jacobian determinant at a particular voxel, the volume of a particular brain structure, or another imaging measure for comparison (such as image intensity). For example, y_{ij} could be the value of the total brain volume for Mouse 3 measured on day 5. $\beta_1,\ldots,\beta_p$ are fixed effects coefficients corresponding to fixed-effect regressors $x_{1ij},\ldots,x_{pij}$. Here, these regressors are *cohort* (whether or not a mouse was scanned on even or odd days) and the scan day itself. b_{iq} and z_{qij} are the random effect coefficients and their regressors, respectively. In the present study, we consider the mouse ID to be a random effect; that is, aside from natural variability within the population, the differences in growth trajectories between mice are effectively random, and we need to account for this in our models. ε_{ij} is the error term, and is assumed to be independent and normally distributed. We can therefore rewrite the above formulation more specifically for our model as:

$$y_{ij} = \beta_1 + \beta_2 c_i + \sum_{k=3}^{l} \beta_k f_k(d_{ij}) + b_{1i} + b_{2i} d_{ij} + \varepsilon_{ij} \quad (4)$$

In Eq. (4), c_i is the cohort (odd or even), which depends only on the mouse i and not the scan day, j. The scan days themselves are denoted d_{ij}. To model growth as a function of time, we used spline interpolation (the *splines* package in R) instead of a simple linear or polynomial fit. This is encapsulated in the term $\sum_{k=3}^{l} \beta_k f_k(d_{ij})$. Each $f_k(d_{ij})$ is the natural spline basis function and β_k is the corresponding coefficient. For example, if we choose to use a natural spline with three degrees of freedom, this sum would expand to:

$$\beta_3 f_3(d_{ij}) + \beta_4 f_4(d_{ij}) + \beta_5 f_5(d_{ij}) \quad (5)$$

In Eqs. (3) and (4), b_{1i} (where $z_{ij} = 1$) is a random effect that corresponds to a separate intercept for each mouse, and b_{2i} (where $z_{ij} = d_{ij}$) is a random effect that allows each slope of the fit to vary for each mouse as well. With these two terms, we can model subtle differences in growth for each mouse, while necessarily separating this random effect from the fixed effects of cohort and day.

Eq. (4) is quite general, and relies on several assumptions. Specifically, we assume that the effect of cohort is significant enough to be included in the model, and we also assume that both a random slope and intercept per subject are needed. In order to validate the appropriateness of these assumptions, as well as make inferences on brain developmental patterns, we explicitly tested them using log-likelihood comparisons of nested models.

As an example of a log-likelihood comparison, consider the Jacobian determinant of a single voxel, measured in all subjects on all days. Alternatively, consider the volume of the hippocampus, measured in all subjects on all scan days. For both of these measurements, we'd like to find the best possible model for growth. To begin, we can compare a linear fit (first order natural spline) to a quadratic fit (second order natural spline). These fits are modeled as:

$$\begin{aligned} y_{ij,Lin} &= \beta_1 + \beta_2 c_i + \beta_3 f_3(d_{ij}) + b_{1i} + b_{2i} d_{ij} + \varepsilon_{ij} \\ y_{ij,Quad} &= \beta_1 + \beta_2 c_i + \beta_3 f_3(d_{ij}) + \beta_4 f_4(d_{ij}) + b_{1i} + b_{2i} d_{ij} + \varepsilon_{ij} \end{aligned} \quad (6)$$

In Eq. (6), *Lin* and *Quad* stand for the linear and quadratic fits respectively. Note that the only difference between them is the presence of the $\beta_4 f_4(d_{ij})$ term in the quadratic equation. To assess how much this additional term improves the model of growth, we use the standard log-likelihood test:

$$-2 \log \frac{L\left(\hat{\theta}_L; \boldsymbol{y}\right)}{L\left(\hat{\theta}_Q; \boldsymbol{y}\right)} \quad (7)$$

In Eq. (7), $L\left(\hat{\theta}_L; \boldsymbol{y}\right)$ is the maximum likelihood of the linear model, subject to a set of optimized parameters $\hat{\theta}_L$. The analogous definition applies for $L\left(\hat{\theta}_Q; \boldsymbol{y}\right)$. Here, the vector $\boldsymbol{y}$ indicates that we are considering the joint probability distribution for all measurements y_{ij} in the construction of L. For example, $\boldsymbol{y}$ could represent the volume of hippocampus, measured for each subject i across multiple days (j). Note that Eq. (7) follows the χ^2 distribution with 1 degree of freedom, which corresponds to the difference in the number of parameters between the two models. From this distribution and the value of the ratio given in Eq. (7), we can find the appropriate p-value for comparing these models. $p < 0.05$ generally indicates that the term in the denominator (in this case, the quadratic model) is a better fit. In every voxel in the brain and for each brain structure we used the log-likelihood test to compare linear and quadratic growth curves, as described here, as well comparing quadratic and cubic growth patterns (second vs third order spline fits) and cubic vs fourth order growth patterns (third vs fourth order).

We can use an identical approach to assess whether each brain region or voxel requires a random intercept per subject or a random intercept plus a random slope per subject. To compare these models, one would simply omit $b_{2i} d_{ij}$ from Eq. (4), which is the term that corresponds to including a random slope. Comparing the resulting equation to Eq. (4) using the log-likelihood test would validate whether or not the random slope is needed.

Software

The core algorithms described in this paper are open source and freely available (overview can be found at http://wiki.mouseimaging.ca). The registration pipelines are implemented in pydpiper (Friedel et al., 2014) (source code: https://github.com/Mouse-Imaging-Centre/pydpiper), and mixed effects models in R (lme4 package (Bates et al., 2014)) are exposed through RMINC (https://github.com/Mouse-Imaging-Centre/RMINC).

Results

Effects of MEMRI on postnatal mouse brain development

To investigate the developmental effects of the longitudinal MEMRI imaging protocol, we acquired daily measurements of the body weights of 4 groups of postnatal mice (groups G1 to G4, N = 14 mice in each group; see Materials and methods section for a detailed description of each group) between P0 and P20 (Suppl. Fig. 1). There was a reduction in the body weights of mice in group G1 (Mn exposure between P0 and P10 and longitudinal MEMRI between P1 and P11) compared to G4 (no Mn or imaging), evident at all stages after P2 ($p < 0.01$ at each stage), peaking close to 20% between P6 and 10 and recovering to 7% by P20. Both Mn-exposure and MRI had significant effects on body weight, since the weight loss in G2 (Mn between P0 and P10 but no MRI) compared to G4 was still significant ($p < 0.05$ at each stage between P6 and 20), but peaking at only 11% (vs 20% for G1) at P8. Interestingly, when Mn-exposure was limited to P0 (G3), there was a similar loss in body weight, compared to G4 ($p < 0.05$, at stages between P4 and 10), again peaking close to 11% at P8, suggesting that much of the Mn-effect was due to exposure at the earliest stage. This was also

supported by the fact that no statistically significant differences were detected between G2 (Mn between P0 and P10) and G3 (Mn only at P0).

To examine the effects of MEMRI on neural development, brain volumes were analyzed at P11 and P21, comparing the mice in our experimental group that were exposed to Mn every other day from P0 to P10 and then again at P20, and imaged 24 h after each Mn exposure (P1–P11 and again at P21; N = 6) to control mice that were only exposed once to Mn at P10 or P20 and imaged 24 h later at P11 (N = 6) or P21 (N = 6). The brains of the experimental mice were about 10% smaller than controls at P11 (335.7 ± 25.8 mm^3 vs 372.4 ± 15.5 mm^3, p = 0.014), a difference that decreased to 6% at P21 (403.3 ± 16.1 mm^3 vs 428.3 ± 11.6 mm^3, p = 0.012) (Suppl. Fig. 2). To investigate more specifically the effect of MEMRI on brain anatomy, we used DBM to compare P11 brains of the experimental and control mice after correcting for differences in overall brain volume (Fig. 3). Altered morphology was detected in only a few small, isolated foci. Specifically, there were small regions of decreased volume in the olfactory bulb (not shown), motor cortex and cerebellum, localized in the crown of lobule IV–V and a region between lobules I and II. These cerebellar lobules are known to be most variable between different mouse strains (Sillitoe and Joyner, 2007), suggesting that they may also be more susceptible to environmental effects. There were also foci of increased volume in the external capsule and just above the interpeduncular nucleus. Interestingly, no regions of altered morphology were detected in the thalamus, the brain region reported to have the largest changes in transition metal homeostasis after MEMRI (Moldovan et al., 2013).

Taken together, our results demonstrated a small but measureable effect on body weight and brain volume during early postnatal development due to the MEMRI protocol, both due to Mn-exposure and anesthesia/MRI. This effect appeared to be transient, with body weight and brain volume both recovering to near normal values by weaning stage. Importantly, the overall morphology of the developing mouse brain was not perturbed in any major way by the imaging protocol. We conclude that MEMRI provides a unique and valuable in vivo approach for studying mouse brain development.

Longitudinal MEMRI of the developing mouse brain

As expected from our previous imaging of the early postnatal mouse brain (Szulc et al., 2013; Wadghiri et al., 2004), MEMRI enhancement was observed in a number of brain regions, most obvious in layers of the cerebellum, hippocampus and olfactory bulbs (Fig. 4; Suppl. Fig. 3). Registration of the data was employed to generate averaged 3D MEMRI images at each stage, which improved the SNR and visibility of finer anatomical details, especially at the earlier developmental stages (Fig. 4; Suppl. Fig. 3). The images were used for quantitative DBM, for 3D segmentation and volumetric analysis, and were also useful for generating 2D (Suppl. Video 1) and 3D (Suppl. Videos 2 and 3) time-lapse animations of normal mouse brain growth, merging the data from each day between P1 and P11 (Fig. 2). Improved visualization of the foliation (folding) patterns in the developing cerebellum was particularly obvious in the averaged images, enabling clearer separation of the individual lobules even at early postnatal stages (before P4) than was possible in images of individual mice (Fig. 4; Suppl. Fig. 3).

In addition to the enhancement of layers in the brain regions described in the previous section, we also observed enhancement in numerous nuclei distributed throughout the brain at each developmental stage, most obvious on the registered and averaged images (Fig. 5). Several axonal fiber tracts were also enhanced, including the vestibulocochlear nerve and the fasciculus retroflexus, which connects the habenular and interpeduncular nuclei. Previously, we used MEMRI signal enhancement to assess morphological and functional phenotypes in the inferior colliculus of *Fgf17* mutant mice (Yu et al., 2011), and to detect and analyze novel morphological phenotypes the cerebellar nuclei of *Gbx2* mutant mice (Szulc et al., 2013). To obtain a more global appreciation of which brain nuclei can be visualized MEMRI, we performed a preliminary annotation of enhanced regions in selected P11 sections (Fig. 5). The results showed that all the brain stem motor nuclei (e.g., oculomotor, trochlear, motor trigeminal, facial, abducens, hypoglossal) were enhanced at P11, as well as many other nuclei at every level of the brain, from olfactory bulbs to brainstem (see Fig. 5 for a detailed list of enhanced nuclei).

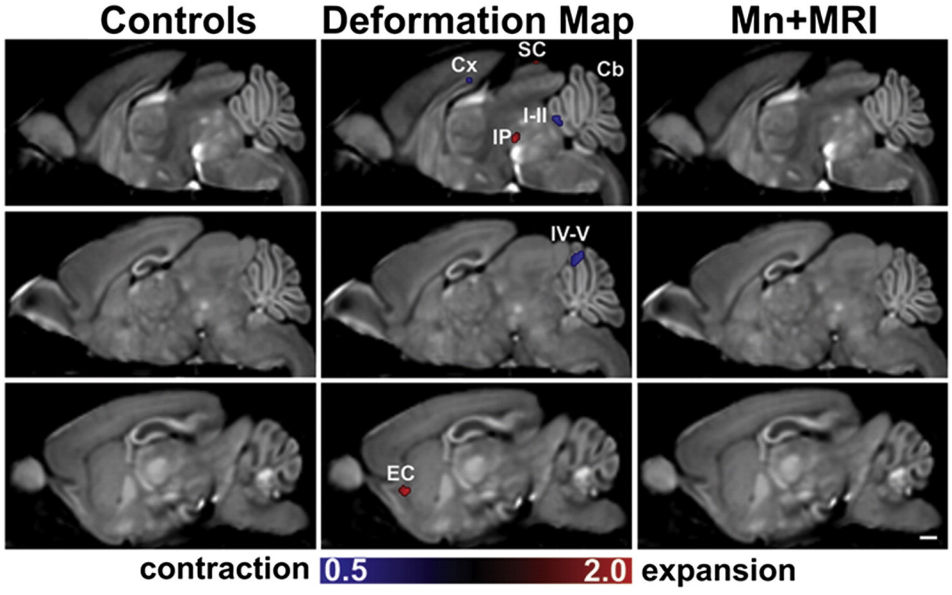

Fig. 3. DBM analysis of the effects of the MEMRI protocol on brain morphology. Matched P11 sagittal images are shown at three levels for the averaged control mice (left panels; mice exposed to Mn only once at P10 and imaged with MRI at P11) and experimental "Mn + MRI" mice (right panels; mice exposed to Mn every other day between P0 and P10 and imaged one day after each Mn-exposure at P1–P11). The deformation maps (middle panels) show statistically significant voxel size differences in color (false discovery rate, FDR < 0.05), superimposed on the average control images. DBM revealed only small focal volume differences, where the color scale indicates regions that were significantly larger (red; volume expansion up to 2×) or significantly smaller (blue; volume contraction down to 0.5×) in the Mn + MRI vs control mice. Labels: Cb, cerebellum; Cx, cortex; EC, external capsule; IP, interpeduncular nucleus; SC, superior colliculus; I–II, cerebellar lobules I–II; IV–V, cerebellar lobules IV–V. Scale bar = 1-mm for all panels.

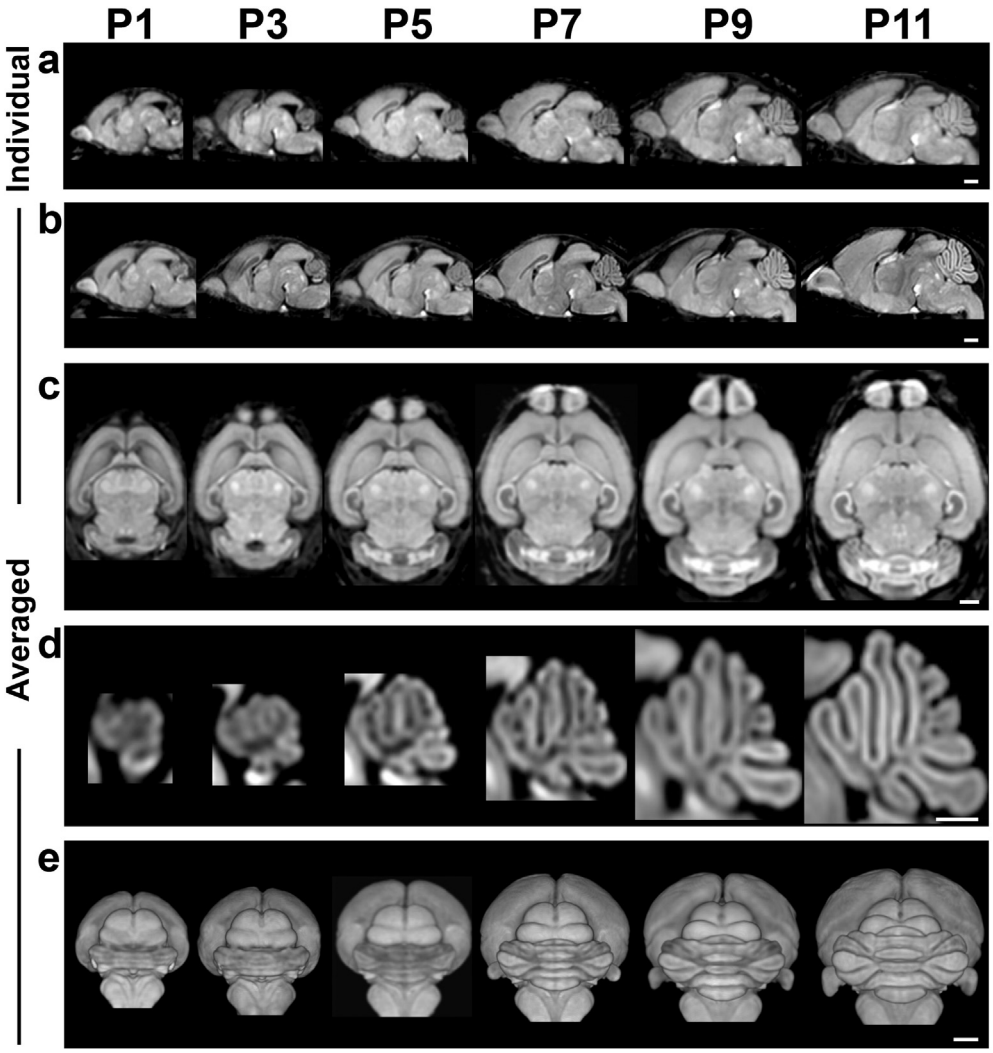

Fig. 4. MEMRI imaging of mouse brain development. MEMRI images are shown of an individual mouse (a) and the registered and averaged images (b,c), every other day from P1 to P11. The growth of the brain over these stages was obvious, with the averaged images providing finer anatomical detail and increased signal-to-noise-ratio (SNR) compared to individual images. Average images are shown in both sagittal (b; see Suppl. Video 1 for 2D movie of average brain growth) and horizontal (c) sections. (d) Magnified sagittal views of the (averaged) cerebellum show the marked changes in morphology and the growth of individual lobules between P1 and P11. (d) Volume renderings, viewed from the back, were effective for visualizing the 3D morphology of the developing cerebellum (see Suppl. Videos 2 and 3 for 3D movies of average brain growth). Scale bar = 1-mm for all panels.

Registration accuracy

To test how accurately brain images could be registered across days, an average image from each day was registered to every other day in the dataset, and the registration accuracy computed by comparing the best available labels for each day to those from each registration. Accurate registrations (Kappa > 0.75) were only obtained within two days for the early scans (P1–P5), but could be obtained over a larger range for later days (P6–P11) (Fig. 6).

4D analysis of developmental brain growth

While it is well accepted that different regions of the brain have distinct growth characteristics, there are few quantitative data available for detailed studies of regional growth during brain development (Calabrese et al., 2013). The 4D MEMRI data set provides an ideal platform for these analyses, containing multiple sets of longitudinal brain images from individual mice, as well as a complete set of registered and averaged 3D images at each stage between P1 and P11. 3D DBM was applied to both individual (every other day) and averaged MEMRI data (every day between P1 and P11) to analyze temporal changes in brain volume on a voxel-by-voxel level (Fig. 7; Suppl. Video 4). As expected, individual mouse brains showed the same general trends as the averaged mouse brain, but with variations in the regional growth rates of up to 10–15% per day, comparing individual and average growth maps. The DBM results provide quantitative measures of brain growth, including the early growth of forebrain regions, such as the olfactory bulbs, cortex and hippocampus, and the relatively late and persistent growth of the cerebellum compared to other brain regions.

To validate the voxel-wise mapping results, the whole brain and selected brain regions (caudate putamen, cerebellum, cortex, hippocampus, inferior colliculus, olfactory bulb and superior colliculus) were segmented from the 4D MEMRI images for analysis of volume as a function of developmental stage (Fig. 8; Suppl. Table 1). Most of the brain regions showed relatively linear growth behavior up to P10, and slower growth between P10 and P11. In the cerebellum, we observed slower growth up to P5, followed by relatively linear growth up to P11. To further assess the differential growth characteristics of different brain regions, the data were fitted to four different linear models at each voxel, using natural splines with increasing degrees of freedom from 1 to 4 (Fig. 9). The resulting maps indicated that 3 degrees of freedom were sufficient for the vast majority of voxels, and that most brain regions were well represented using only 1 or 2 degrees of freedom, the

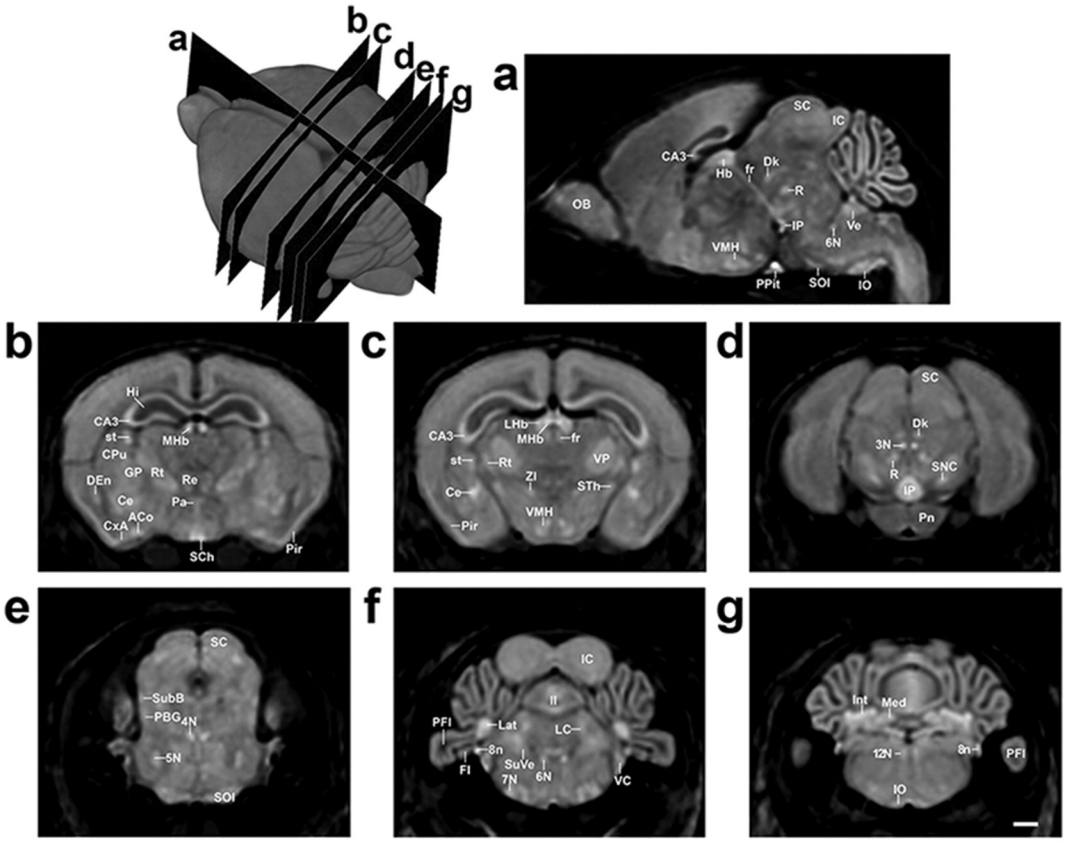

12N	hypoglossal nucleus	LHb	lateral habenular nucleus
II	lobule 2 of the cerebellar vermis	Med	medial cerebellar nucleus
3N	oculomotor nucleus	MHb	medial habenular nucleus
4N	trochlear nucleus	OB	olfactory bulb
5N	motor trigeminal nucleus	Pa	paraventricular nucleus of the hypothalamus
6N	abducens nucleus	PBG	parabigeminal nucleus
7N	facial nucleus	PFl	paraflocculus
8n	vestibulocochlear nerve	Pir	piriform cortex
ACo	anterior cortical amigdaloid nucleus	Pn	pontine nuclei
CA3	field ca3 of the hippocampus	R	red nucleus
Ce	central amygdaloid nucleus	Re	reuniens thalamic nucleus
CPu	caudate putamen (striatum)	Rt	reticular nucleus
CxA	cortex-amygdala transition zone	SC	superior colliculus
DEn	dorsal endopiriform nucleus	SCh	suprachiasmatic nucleus
Dk	nucleus of darkschewitsch	SNC	substantia nigra
Fl	flocculus	SOl	superior olive lateral
fr	fasciculus retroflexus	st	stria terminalis
GP	globus pallidus	STh	subthalamic nucleus
Hb	habenular	SubB	subbrachial nucleus
Hi	hippocampus	SuVe	superior vestibular nucleus
IC	internal capsule	VC	ventral cochlear
Int	interposed cerebellar nucleus	Ve	vestibular nuclei
IO	inferior olivary nucleus	VMH	ventral medial nucleus of the hypothalamus
IP	interpeduncular nucleus	VP	ventroposterior nucleus of thalamus
Lat	lateral (dentate) cerebellar nucleus	ZI	zona incerta
LC	locus coeruleus		

Fig. 5. MEMRI revealed enhancement of numerous nuclei in the developing brain. MEMRI resulted in marked enhancement of numerous tissue layers, brain nuclei and axonal tracts, which could provide valuable anatomical landmarks in a future atlas of mouse brain development. Annotation of the enhancing brain regions was performed in selected sagittal (a) and coronal (b–g) sections of the average P11 brain (insert shows the approximate location of each of the sections). The legend below the image panels defines the labels shown on the MEMRI images. Scale bar = 1-mm for all panels.

cerebellum being the clearest example of a region that was best fit by 3 degrees of freedom.

Analysis with two distinct mixed-effects models enabled us to assess individual variability in regional brain growth (Fig. 10). To identify these brain regions, statistical voxel-wise maps were generated to show where the image time-course was fit better by Model 1 (which included only a random intercept term for each mouse) or where it was fit better by Model 2 (which included both a random intercept and slope—growth rate—term for each mouse). We identified the hippocampus and cerebellum as the regions where the observed growth was most variable between individuals (Fig. 10a). Region-of-interest analyses were also performed, covering a number of 3D brain regions

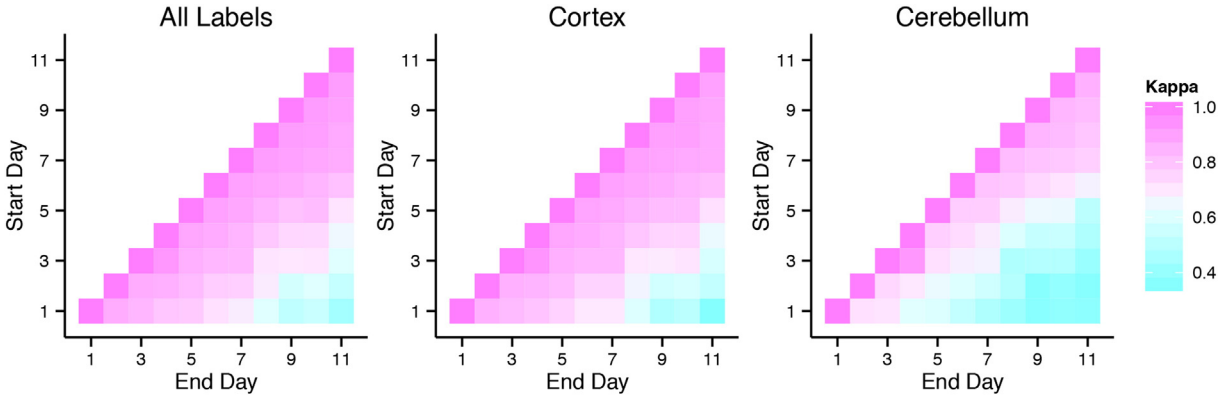

Fig. 6. Registration accuracy. The accuracy of registering images from different postnatal stages are illustrated for all 7 labels combined as well as the cerebral cortex and the cerebellum individually, with the colors indicating the Kappa statistics obtained. A P1 scan, for example, can be aligned with reasonable accuracy in the cerebellum to P2 and P3, but not to later stages, whereas the cerebellum in a P7 scan can be aligned accurately to P8–P11. Cortical alignment across days has increased accuracy compared to cerebellar alignment.

(Fig. 10b,c). The results showed that Model 2 provided a better fit than Model 1 for most brain regions, with the largest effect observed in the cerebellar lobules (Fig. 10c).

Quantitative analysis of cerebellum development

The previously described growth analyses (Figs. 7, 8) demonstrated that the cerebellum develops later than most other brain regions, and undergoes significant morphological changes over the temporal window of the current studies. Recent evidence suggests that in addition to the obvious advantage of increasing the surface area per unit volume, the cerebellar lobules act as scaffolds to organize neural circuits during development (Fujita and Sugihara, 2013; Sillitoe et al., 2010; Stoodley et al., 2012). We therefore investigated further the lobule-specific developmental growth patterns. Each vermis lobule was segmented in the average P11 image and mapped to each individual mouse and stage. Similar to the previous volumetric analysis of whole cerebellum (Fig. 8b), the cerebellar lobules generally grew slowly in the earlier stages, followed by a period of more rapid growth after P4–P5 (Fig. 11a,b; Suppl. Table 1). This was most obvious in the anterior lobules IV–V and the posterior lobules IX and X.

In addition to analysis of lobule morphology and growth, MEMRI also provided detailed visualization of the cerebellar nuclei, the primary output nuclei of the cerebellum (Fig. 11c,d). Specifically, the medial (fastigial), interposed and lateral (dentate) cerebellar nuclei were segmented from MEMRI images at each developmental stage using the registration data (Fig. 11c), and these segmentations were used to analyze the volumetric changes in each nucleus, as a function of developmental stage. The results showed that the medial nucleus had a significantly slower growth rate compared to the interposed and lateral nuclei (Fig. 11d).

The developmental brain images acquired in this study can also be used to address fundamental biological questions related to cerebellar morphogenesis. Recently, it was proposed that during cerebellar development the base of each fissure remains relatively stationary—acting like an "anchoring center"—with growth of each folia is directed outwards from these anchoring centers (Sudarov and Joyner, 2007). We tested this hypothesis by placing markers at the base (anchoring center) and crown of selected lobules in the averaged P11 image, and using the

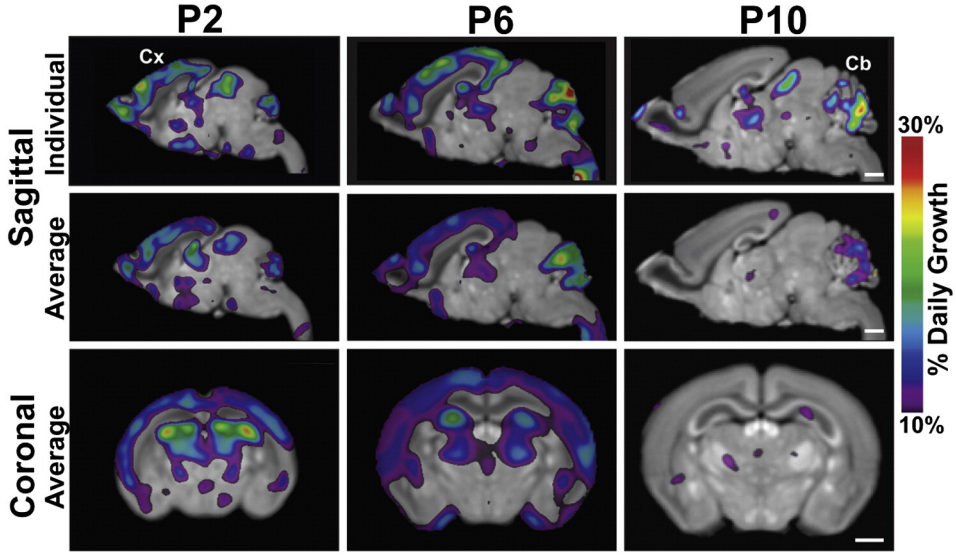

Fig. 7. DBM analysis of volumetric growth in the developing brain. Time-series DBM analysis was performed on individual and averaged images to determine the stage-dependent changes in voxel volume. Individual sagittal (top row), average sagittal (middle row), and average coronal (bottom row) sections are shown at postnatal days P2, P6 and P10, with the DBM map superimposed in color on the averaged images at each stage (false discovery rate, FDR < 0.05; color shows changes between 10% and 30% of daily brain growth, color scale included in insert). Daily brain growth was calculated by taking the current time plus half a day minus the current time minus half a day, divided by the current minus half a day. Note the early pronounced growth in the cortex (Cx), and the later, more prolonged growth of the cerebellum (Cb) compared to other brain regions (see Suppl. Video 4 for a mid-sagittal movie of the DBM results). Scale bars = 1-mm for all panels in each row.

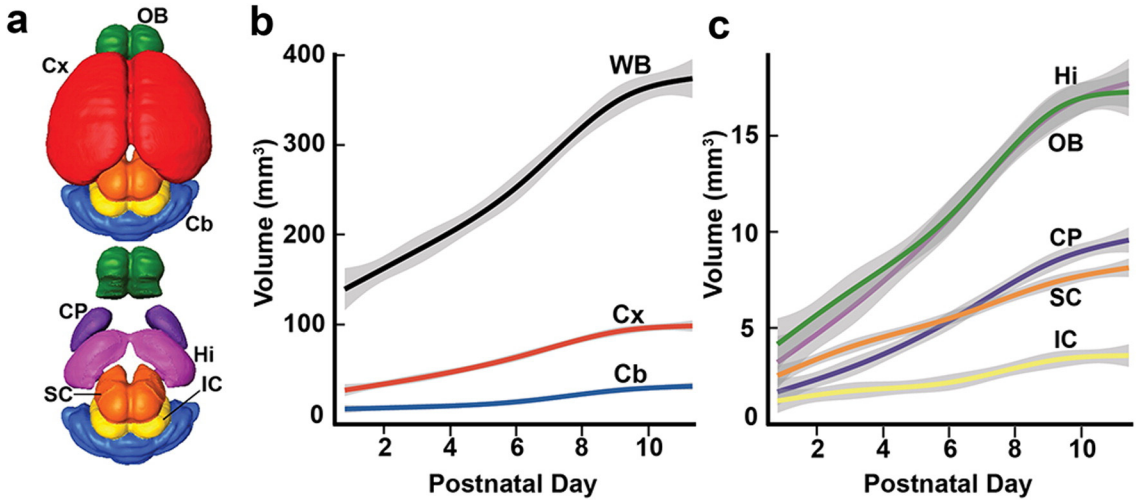

Fig. 8. Volumetric analysis of selected brain regions. (a) Selected brain regions were segmented and analyzed at each developmental stage: Cb, cerebellum; CP, caudate putamen; Cx, cortex; Hi, hippocampus; IC, inferior colliculus; OB, olfactory bulb; SC, superior colliculus; WB, whole brain. (b, c) The curve for each region shows the mean volume, fitted to a third order spline, and plotted as a function of postnatal stage from P1 to P11. The shaded areas represent the 95% confidence intervals. ($^{*}p < 0.05$).

transforms generated by the registrations to map the markers (i.e., transform the marker coordinates) to earlier developmental stages (Fig. 12; Suppl. Video 5). Quantitative analysis confirmed that the putative anchoring centers remained relatively stationary compared to the cerebellar center (chosen arbitrarily at P11 and mapped back through the registrations). As predicted, the major growth of the cerebellum was generated along the length of the lobules, outward from the stationary anchoring centers. Specifically, between P1 and P11 the mean distance from the cerebellar center to the anchoring centers increased from 0.25 ± 0.05 mm to 0.42 ± 0.1 mm, while the mean distance from the cerebellar center to the crowns increased from 0.72 ± 0.1 mm to 1.6 ± 0.3 mm over the same period.

Discussion

This study demonstrates the feasibility of longitudinal neuroimaging in neonatal mice starting as early as P1. MEMRI was employed for imaging neonatal brains between P1 and P11, with Mn delivery to the mouse pups via lactation after a maternal IP injection of $MnCl_2$ solution (Szulc et al., 2013). Use of the MEMRI protocol provided contrast at all developmental stages between P1 and P11, enabling visualization of multiple brain regions and nuclei, sufficient for qualitative and quantitative in vivo analyses over the first 11 days after birth. In combination with our previous in utero results in mid- to late-fetal stage mice (Deans et al., 2008), this study establishes MEMRI as a unique and powerful

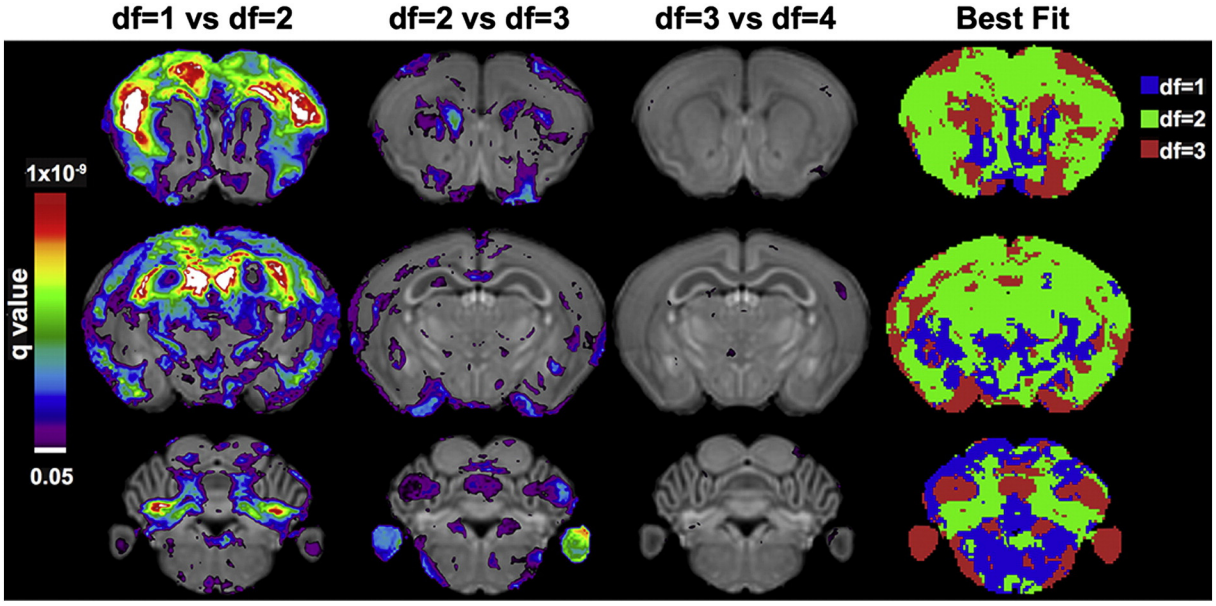

Fig. 9. Assessing which models best describe regional brain development. Developmental MEMRI data were fitted to four different linear models at each voxel, using natural splines with increasing degrees of freedom (df = 1 to 4). At each voxel, the models were then compared statistically. The first column shows areas of the brain where a spline with two degrees of freedom (df = 2) provided a significantly better fit than a spline with a single degree of freedom (df = 1, i.e. a line). The next column compares two degrees of freedom to three degrees of freedom (df = 2 vs df = 3), and the third column three vs four degrees of freedom (df = 3 vs df = 4). The color bar shows the q-value, from 10^{-9} to 0.05 on a -log10 scale. The final column shows the resulting map of the best fitting degrees of freedom (df = 1, blue; df = 2, green; df = 3, red).

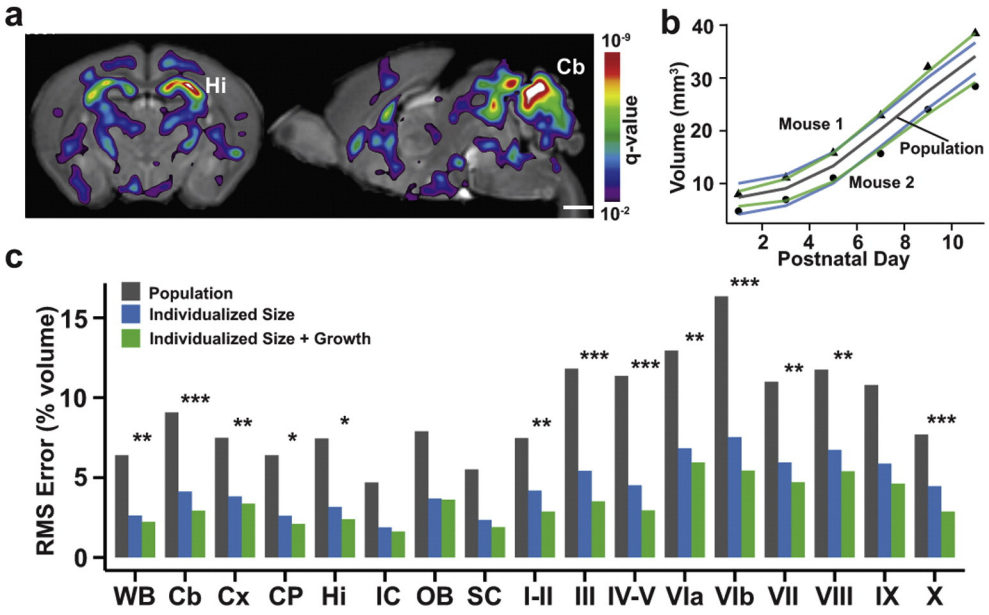

Fig. 10. Analysis of region-specific variability in brain growth. (a) Two linear mixed-effect models were compared statistically, to assess in each voxel whether the P1–P11 data was best fit by a model using only separate intercepts for each mouse (Model 1: allows for differences in size between individuals) or a model using separate intercepts and slopes for each mouse (Model 2: allows for differences in size and growth rate between individuals). The resulting q-values (color bar shown in insert) were superimposed on P11 coronal and sagittal images, identifying the hippocampus and cerebellum as two regions where growth was highly individualized. (b) Cerebellum volume was plotted as a function of postnatal day, between P1 and P11, showing the population average (gray line) and data from two individuals, one above (triangles) and one below (circles) the population average. For both mice, Model 2 (green) provided a better fit to the data than Model 1 (blue). (c) The root-mean-square (RMS) error was calculated for the same brain regions (Cb, cerebellum; CP, caudate putamen; Cx, cortex; Hi, hippocampus; IC, inferior colliculus; OB, olfactory bulb; SC, superior colliculus; WB, whole brain) and cerebellar lobules (I–II, III, IV–V, VIa, VIb, VII, VIII, IX, X), expressing the results as a percentage of the region's volume. The results show smaller RMS errors, comparing either of the mixed-effect models to the population average (gray bars), and generally show smaller errors for Model 2 compared to Model 1. These differences were assessed statistically using log-likelihood tests, showing that all brain regions were better fit using Model 2, except for the IC, SC, OB and lobule IX, and that Model 2 had the greatest effect in the cerebellum ($^{*}q < 0.05$; $^{**}q < 0.01$; $^{***}q < 0.0001$). Scale bar = 1-mm for panel (a).

approach for in vivo neuroimaging from neural tube closure through the critical neonatal stages of mouse brain development.

One of the challenges of longitudinal brain imaging was the acquisition of motion artifact free data in multiple imaging sessions for each individual neonatal mouse. This challenge was met using a combination of stage-specific silicone holders, molded to the bodies and heads of the neonatal mice to prevent large displacements, together with a self-gated acquisition sequence for real-time monitoring of respiratory motion and retrospective elimination of corrupted k-space lines prior to image reconstruction (Nieman et al., 2009). Real-time monitoring, via the self-gated sequence, was found to be essential during the long (2 h) acquisition periods, allowing adjustments to anesthesia levels and warm air temperature to maintain a constant respiratory rate indicative of proper health and physiology of the neonatal animals. The breathing rate maintained during imaging in these studies (30 breaths/min) was relatively low compared to that of normal awake mice, especially at post-weaning stages. However, in our experience this breathing rate, combined with low levels of isoflurane anesthesia (0.5–1% in air), was very safe for the neonatal mice during the 2 h scan times, and resulted in minimal motion artifacts and excellent image quality. We note also that our gradient echo sequence retains sufficient sensitivity to hypoxia and that we have observed hypoxia-related artifact in image acquisitions previously. This was not observed for any of the mice imaged in this study.

Novel registration-based mapping methods, using intermediate atlases and transform concatenations, were also developed for time-series analysis of stage-to-stage changes in neuro-anatomy. Time-series analyses were performed on MEMRI data, using both voxel- and region-based methods that enabled characterization of developmental changes in voxel and regional volumes. The ability to perform automated segmentations of numerous brain regions across a wide range of developmental stages was a particularly important feature of this study, enabling quantitative analyses of volume changes in multiple brain regions, with sizes from the whole brain down to individual lobules and nuclei in the cerebellum. Automated segmentation was also adapted to track small regions in the cerebellum, to address fundamental questions related to the process of cerebellar foliation. Given the growing use of MEMRI for small-animal anatomical (Gazdzinski et al., 2012; Qiu et al., 2013; Szulc et al., 2013), functional (Cacace et al., 2014; Chan et al., 2014; Yu et al., 2005) and molecular (Bartelle et al., 2013) neuroimaging, these results should provide important background data for future analyses of brain development on multiple levels, in both normal mice and a variety of mutants.

Results of our analyses nicely corroborate developmental neurobiology findings that the cerebellum is indeed the region showing the most pronounced post-natal growth and our ability to quantify cerebellar volume changes and rates of growth on a lobule by lobule basis will be particularly useful for anatomical phenotyping of mouse mutants with specific cerebellar foliation defects such as Engrailed 2 (*En2*) and/or Engrailed 1 (*En1*) conditional mutant mice (Cheng et al., 2010; Orvis et al., 2012). The additional capability of analyzing cerebellar nuclei growth should provide important new insights on this critical center of cerebellar circuitry (Szulc et al., 2013). Previously, it was shown that cerebellar foliation development begins with establishment of multicellular anchoring centers at the base of the fissures that were suggested to remain stationary throughout the process of cerebellar development (Sudarov and Joyner, 2007). By using registration-based image analysis methods, we were able to provide a quantitative validation of the idea that the base of each fissure indeed functions as an anchoring center by remaining relatively stationary during development and while the tips of the folia grow outward from each base. The ability to quantify folia base and tip position, as well as individual lobule growth rates, now provides an important new method for analyzing cerebellar foliation defects in mouse mutants.

Because of the in vivo longitudinal design of our studies, we were able to identify brain regions characterized by individualized growth patterns. This type of analysis would be impossible using ex vivo imaging or other cross-sectional study designs. Our hypothesis is that brain

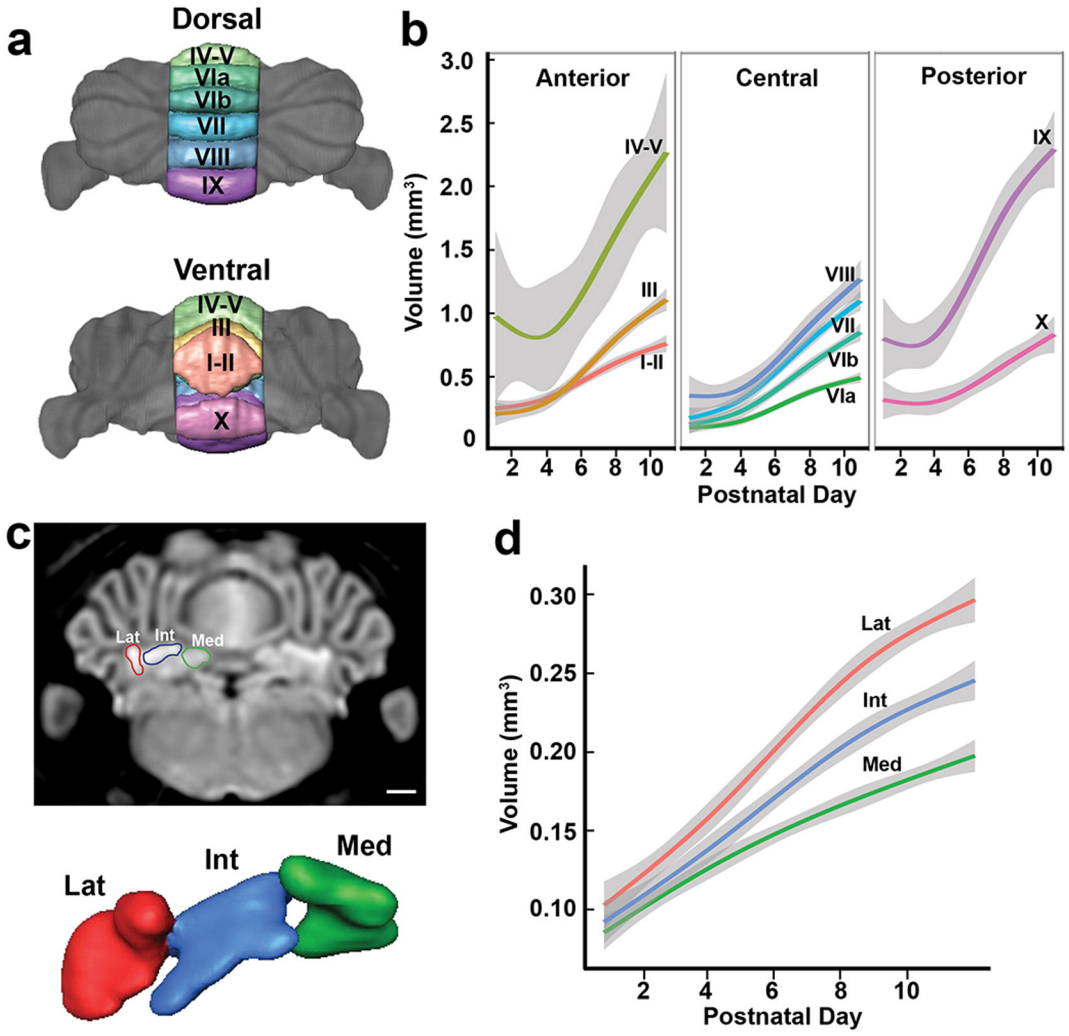

Fig. 11. Analysis of cerebellar nuclei development. (a) The cerebellar lobules (I–II, III, IV–V, Via, VIb, VII, VIII, IX, X) were segmented from MEMRI data and (b) volumetric growth curves were computed for each lobule between P1 and P11 (mean values shown by solid curves, 95% confidence intervals shown in shaded regions). A similar analysis was also performed to (c) segment and (d) measure the volumetric growth curves for the three separate cerebellar nuclei: medial (Med, green); interposed (Int, blue); and lateral (Lat, red). Scale bar = 1-mm for panel (c).

regions like the hippocampus and cerebellum, identified in this analysis, are particularly susceptible to environmental influences and epigenetic regulation. This result is consistent with previous reports in the literature that hippocampal mossy fiber areas CA1 and CA3 are highly influenced by the level of maternal care and other early postnatal environmental factors, with possible mediation by epigenetic mechanisms (Kaffman and Meaney, 2007; Kappeler and Meaney, 2010; Meaney, 2001; Meaney et al., 2002; Szyf et al., 2005). The experiments in this paper necessarily involved maternal separation during MRI, potentially increasing inter individual differences in response to this stressor. Select cerebellar lobules show the most pronounced individualized growth patterns. In addition, brain regions sending modulatory projections (substantia nigra, locus coeruleus, septum, histaminergic neurons of the tuberomammillary nucleus) also showed individualized growth patterns.

It is worth discussing some of the limitations of registration-based analyses and MEMRI studies in general. One caveat that must be appreciated is that analyses of volume and intensity changes are only as accurate as the registration method employed. Registration accuracy of these algorithms has been previously assessed (Badea et al., 2012; Klein et al., 2009; Spring et al., 2007; van Eede et al., 2013) and shown to be able to detect subtle alterations (5% or less) in anatomy between mice as well as accurately segmenting anatomical brain regions (Chakravarty et al., 2013). Structure-wise analyses of brain regions, after automated segmentation, should be less sensitive to errors than voxel-wise analyses, with both methods showing promise for detecting and analyzing mutant phenotypes in the developing mouse brain (Szulc et al., 2013).

MEMRI involves exposing the neonatal mice to Mn and anesthesia, both of which could affect the normal trajectories of brain development. It is well-established that Mn exposure at high doses, can have neurotoxic effects (Bock et al., 2008; Deans et al., 2008; Grunecker et al., 2010; Shukakidze et al., 2003; Silva et al., 2004). Most of the studies assessing toxic effects of Mn are performed with 1–8 repeated injections in 24–48 h intervals to achieve cumulative doses of 180–240 mg/kg of $MnCl_2$ (Bock et al., 2008; Grunecker et al., 2010) or 30 days of 20–50 mg/kg/day $MnCl_2$ in feed (Shukakidze et al., 2003). Even though higher doses than the ones used here have been reported for neuroimaging studies without significant toxicity (Silva et al., 2004), one must take into account the repeated exposure of the neonates to Mn at potentially vulnerable early postnatal stages. Additionally, in this study no injections were performed to the developing pups and instead lactating females were injected every other day from P0 to P10 (6×) or P1 to P9 (5×). The pups received Mn with milk, which is more similar to continuous Mn delivery via osmotic pumps that have been reported to have fewer side effects than acute IP injections (Eschenko et al., 2010; Mok

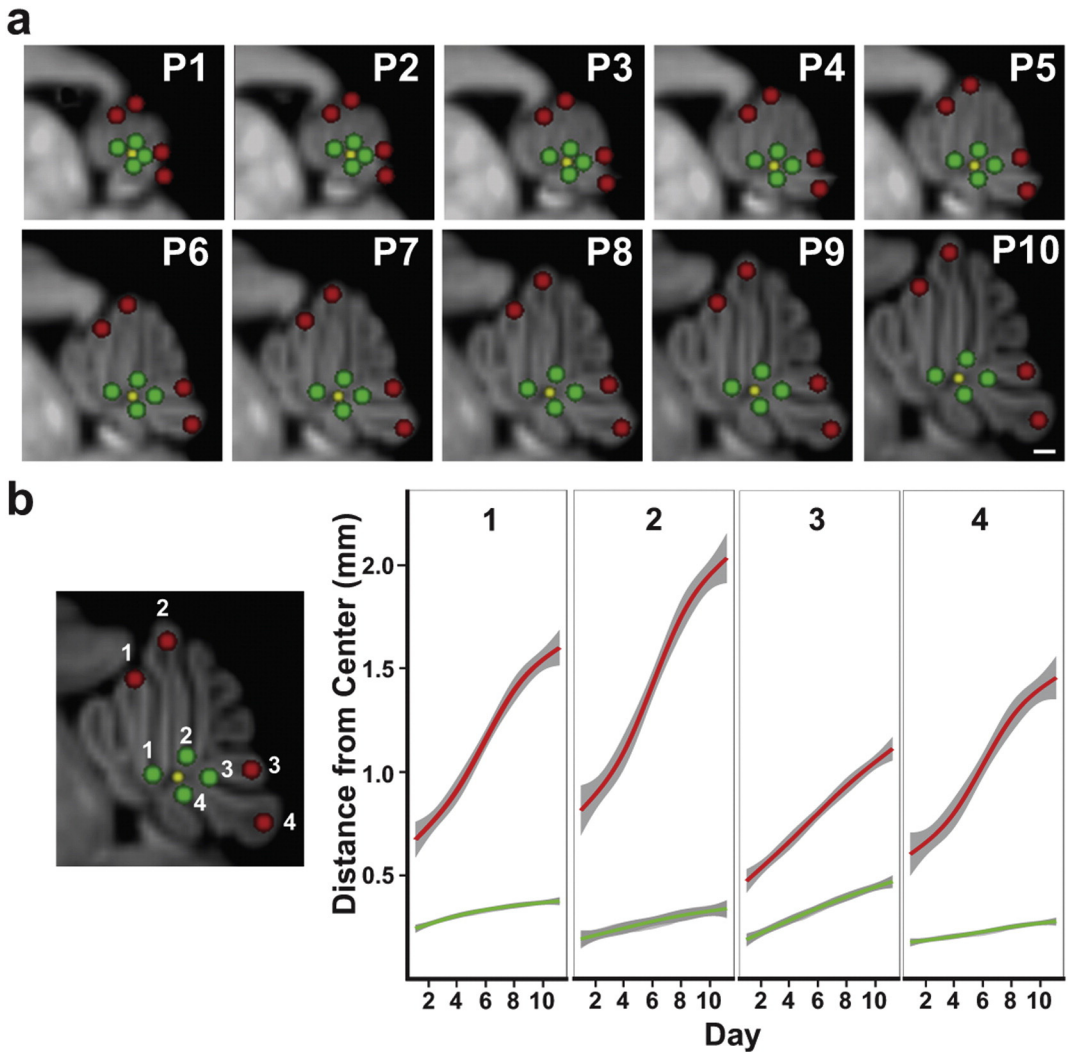

Fig. 12. Analysis of differential outward growth within cerebellar lobules. The registered and averaged MEMRI data was used to test the hypothesis that the base of each fissure represents a stationary anchoring center, and to quantify the differential growth of selected cerebellar lobules. (a) At P11, four putative anchoring centers (1,2 anterior; 3,4 posterior) were marked (green spheres), as well as the tips of a lobule adjacent to each anchoring center (1 = III; 2 = IV–V; 3 = VIII; 4 = IX; see insert). These points were tracked automatically through the time-series registration to each of the earlier stages from P1 to P10, showing relatively small changes in the positions of the green points compared to the yellow point, whereas the red points moved outward (see Suppl. Video 4 for a movie of the tracking results). (b) To quantify these differences, the distance from the cerebellum center (yellow sphere) to each of the green and red points was plotted as a function of postnatal stage from P1 to P11. Scale bar = 0.5-mm in panel (a).

et al., 2012; Sepulveda et al., 2012). Also relevant are studies reporting that fractionated Mn delivery can reduce toxicity (Bock et al., 2008; Grunecker et al., 2010).

In the current study, a careful assessment was made of the effects of the experimental protocol on neonatal brain volume and body weight. The results showed a small but significant effect of longitudinal MEMRI on both body weight and brain volume, but the differences between mice undergoing MEMRI and control mice were significantly reduced at P21 compared to P11 (after which MEMRI was stopped), suggesting that the developmental effects were transient. Interestingly, when the effects of Mn alone were assessed, independent of anesthesia and MRI, the results indicated that most of the growth delay was due to Mn exposure at the earliest developmental stage. In addition, registration-based DBM analysis identified only very small isolated regions where volume changes were localized, indicating that the overall morphology of the neonatal brain was not affected by the longitudinal MEMRI protocol, at least within the statistical power of the current study. Nevertheless, the potential for Mn or anesthesia toxicity, compounded by the stress of maternal separation, is a potential confound that must be taken into account in future studies, especially if they involve lines of mice modeling neurodevelopmental disorders.

In summary, we have demonstrated that quantitative analysis of neonatal mouse brain development is possible using in vivo longitudinal MEMRI data. The ability to perform automated, registration-based segmentations throughout the times-series MRI data enabled efficient characterization of brain development, limiting the work of segmentation to a single stage. A complete annotation of enhanced nuclei and other brain structures will provide anatomical landmarks at each stage and level of the brain, and will increase the utility of the data set for 4D studies of normal and mutant brain development. In the future, it would be interesting to assess the differences between different inbred mouse strains, especially for analysis of mutants where it is critical to distinguish between differences in genetic background from the putative mutant phenotypes under investigation. We intend to use the in vivo images presented in this paper to develop an online 4D atlas of mouse brain development. This will enable growth characterization of a larger number brain structures (similar to the analysis presented for the cerebellar lobules and nuclei), and should aid in future MEMRI experiments of mutant mice with specific developmental brain defects.

Supplementary data to this article can be found online at http://dx.doi.org/10.1016/j.neuroimage.2015.05.029.

Acknowledgments

This research was supported by NIH grants R01NS038461 (DHT) and R37MH085726 (ALJ) and by the Ontario Brain Institute's Province of Ontario Neurodevelopmental Disorders Network (JPL). MRI imaging was partially supported by the Small Animal Imaging Core at NYU School of Medicine, and the NYU Cancer Institute through the NIH Cancer Center Support Grant (P30CA016087). We thank Benjamin Turnbull for assisting with the segmentation and analysis of the cerebellar nuclei.

References

Avants, B., Grossman, M., Gee, J., 2006. Symmetric Diffeomorphic Image Registration: Evaluating Automated Labeling of Elderly and Neurodegenerative Cortex and Frontal Lobe. In: Pluim, J.W., Likar, B., Gerritsen, F. (Eds.), Biomedical Image Registration. Springer, Berlin Heidelberg, pp. 50–57.

Avants, B.B., Epstein, C.L., Grossman, M., Gee, J.C., 2008. Symmetric diffeomorphic image registration with cross-correlation: evaluating automated labeling of elderly and neurodegenerative brain. Med. Image Anal. 12, 26–41.

Badea, A., Gewalt, S., Avants, B.B., Cook, J.J., Johnson, G.A., 2012. Quantitative mouse brain phenotyping based on single and multispectral MR protocols. NeuroImage 63, 1633–1645.

Bartelle, B.B., Szulc, K.U., Suero-Abreu, G.A., Rodriguez, J.J., Turnbull, D.H., 2013. Divalent metal transporter, DMT1: a novel MRI reporter protein. Magn. Reson. Med. 70, 842–850.

Bates, D., Maechler, M., Bolker, B., Walker, S., 2014. lme4: Linear mixed-effects models using Eigen and S4. R Package Version 1pp. 1–4.

Bock, N.A., Paiva, F.F., Silva, A.C., 2008. Fractionated manganese-enhanced MRI. NMR Biomed. 21, 473–478.

Boretius, S., Frahm, J., 2011. Manganese-enhanced magnetic resonance imaging. Methods Mol. Biol. 771, 531–568.

Cacace, A.T., Brozoski, T., Berkowitz, B., Bauer, C., Odintsov, B., Bergkvist, M., Castracane, J., Zhang, J., Holt, A.G., 2014. Manganese enhanced magnetic resonance imaging (MEMRI): a powerful new imaging method to study tinnitus. Hear. Res. 331, 49–62.

Calabrese, E., Badea, A., Watson, C., Johnson, G.A., 2013. A quantitative magnetic resonance histology atlas of postnatal rat brain development with regional estimates of growth and variability. NeuroImage 71, 196–206.

Chakravarty, M.M., Steadman, P., van Eede, M.C., Calcott, R.D., Gu, V., Shaw, P., Raznahan, A., Collins, D.L., Lerch, J.P., 2013. Performing label-fusion-based segmentation using multiple automatically generated templates. Hum. Brain Mapp. 34, 2635–2654.

Chan, K.C., Fan, S.J., Chan, R.W., Cheng, J.S., Zhou, I.Y., Wu, E.X., 2014. In vivo visuotopic brain mapping with manganese-enhanced MRI and resting-state functional connectivity MRI. NeuroImage 90, 235–245.

Cheng, Y., Sudarov, A., Szulc, K.U., Sgaier, S.K., Stephen, D., Turnbull, D.H., Joyner, A.L., 2010. The Engrailed homeobox genes determine the different foliation patterns in the vermis and hemispheres of the mammalian cerebellum. Development 137, 519–529.

Cohen, J., 1960. A coefficient of agreement for nominal scales. Educ. Psychol. Meas. 20, 37–46.

Collins, D.L., Pruessner, J.C., 2010. Towards accurate, automatic segmentation of the hippocampus and amygdala from MRI by augmenting ANIMAL with a template library and label fusion. NeuroImage 52, 1355–1366.

Collins, F.S., Rossant, J., Wurst, W., 2007. A mouse for all reasons. Cell 128, 9–13.

Crawley, J.N., 2012. Translational animal models of autism and neurodevelopmental disorders. Dialogues Clin. Neurosci. 14, 293–305.

Cryan, J.F., Holmes, A., 2005. The ascent of mouse: advances in modelling human depression and anxiety. Nat. Rev. Drug Discov. 4, 775–790.

Deans, A.E., Wadghiri, Y.Z., Berrios-Otero, C.A., Turnbull, D.H., 2008. Mn enhancement and respiratory gating for in utero MRI of the embryonic mouse central nervous system. Magn. Reson. Med. 59, 1320–1328.

Eschenko, O., Canals, S., Simanova, I., Beyerlein, M., Murayama, Y., Logothetis, N.K., 2010. Mapping of functional brain activity in freely behaving rats during voluntary running using manganese-enhanced MRI: implication for longitudinal studies. NeuroImage 49, 2544–2555.

Friedel, M., van Eede, M.C., Pipitone, J., Chakravarty, M.M., Lerch, J.P., 2014. Pydpiper: a flexible toolkit for constructing novel registration pipelines. Front. Neuroinf. 8.

Fujita, H., Sugihara, I., 2013. Branching patterns of olivocerebellar axons in relation to the compartmental organization of the cerebellum. Front. Neural Circ. 7, 3.

Gazdzinski, L.M., Cormier, K., Lu, F.G., Lerch, J.P., Wong, C.S., Nieman, B.J., 2012. Radiation-induced alterations in mouse brain development characterized by magnetic resonance imaging. Int. J. Radiat. Oncol. Biol. Phys. 84, e631–e638.

Grunecker, B., Kaltwasser, S.F., Peterse, Y., Samann, P.G., Schmidt, M.V., Wotjak, C.T., Czisch, M., 2010. Fractionated manganese injections: effects on MRI contrast enhancement and physiological measures in C57BL/6 mice. NMR Biomed. 23, 913–921.

Inoue, T., Majid, T., Pautler, R.G., 2011. Manganese enhanced MRI (MEMRI): neurophysiological applications. Rev. Neurosci. 22, 675–694.

Johnson, G.A., Cofer, G.P., Fubara, B., Gewalt, S.L., Hedlund, L.W., Maronpot, R.R., 2002a. Magnetic resonance histology for morphologic phenotyping. J. Magn. Reson. Imaging 16, 423–429.

Johnson, G.A., Cofer, G.P., Gewalt, S.L., Hedlund, L.W., 2002b. Morphologic phenotyping with MR microscopy: the visible mouse. Radiology 222, 789–793.

Kaffman, A., Meaney, M.J., 2007. Neurodevelopmental sequelae of postnatal maternal care in rodents: clinical and research implications of molecular insights. J. Child Psychol. Psychiatry 48, 224–244.

Kappeler, L., Meaney, M.J., 2010. Epigenetics and parental effects. Bioessays 32, 818–827.

Klein, A., Andersson, J., Ardekani, B.A., Ashburner, J., Avants, B., Chiang, M.-C., Christensen, G.E., Collins, D.L., Gee, J., Hellier, P., Song, J.H., Jenkinson, M., Lepage, C., Rueckert, D., Thompson, P., Vercauteren, T., Woods, R.P., Mann, J.J., Parsey, R.V., 2009. Evaluation of 14 nonlinear deformation algorithms applied to human brain MRI registration. NeuroImage 46, 786–802.

Koretsky, A.P., Silva, A.C., 2004. Manganese-enhanced magnetic resonance imaging (MEMRI). NMR Biomed. 17, 527–531.

Laird, N.M., Ware, J.H., 1982. Random-effects models for longitudinal data. Biometrics 38, 963–974.

Meaney, M.J., 2001. Maternal care, gene expression, and the transmission of individual differences in stress reactivity across generations. Annu. Rev. Neurosci. 24, 1161–1192.

Meaney, M.J., Brake, W., Gratton, A., 2002. Environmental regulation of the development of mesolimbic dopamine systems: a neurobiological mechanism for vulnerability to drug abuse? Psychoneuroendocrinology 27, 127–138.

Mok, S.I., Munasinghe, J.P., Young, W.S., 2012. Infusion-based manganese-enhanced MRI: a new imaging technique to visualize the mouse brain. Brain Struct. Funct. 217, 107–114.

Moldovan, N., Al-Ebraheem, A., Miksys, N.A., Farquharson, M.J., Bock, N.A., 2013. Altered transition metal homeostasis in mice following manganese injections for manganese-enhanced magnetic resonance imaging. Biometals 26, 179–187.

Mori, S., Itoh, R., Zhang, J., Kaufmann, W.E., van Zijl, P.C., Solaiyappan, M., Yarowsky, P., 2001. Diffusion tensor imaging of the developing mouse brain. Magn. Reson. Med. 46, 18–23.

Nieman, B.J., Turnbull, D.H., 2010. Ultrasound and magnetic resonance microimaging of mouse development. Methods Enzymol. 476, 379–400.

Nieman, B.J., Szulc, K.U., Turnbull, D.H., 2009. Three-dimensional, in vivo MRI with self-gating and image coregistration in the mouse. Magn. Reson. Med. 61, 1148–1157.

Nieman, B.J., Wong, M.D., Henkelman, R.M., 2011. Genes into geometry: imaging for mouse development in 3D. Curr. Opin. Genet. Dev. 21, 638–646.

Orvis, G.D., Hartzell, A.L., Smith, J.B., Barraza, L.H., Wilson, S.L., Szulc, K.U., Turnbull, D.H., Joyner, A.L., 2012. The engrailed homeobox genes are required in multiple cell lineages to coordinate sequential formation of fissures and growth of the cerebellum. Dev. Biol. 367, 25–39.

Pautler, R.G., 2004. In vivo, trans-synaptic tract-tracing utilizing manganese-enhanced magnetic resonance imaging (MEMRI). NMR Biomed. 17, 595–601.

Pautler, R.G., 2006. Biological applications of manganese-enhanced magnetic resonance imaging. Methods Mol. Med. 124, 365–386.

Pinheiro, J., Bates, D., 2000. Mixed-Effects Models in S and S-PLUS. Springer.

Qiu, L.R., Germann, J., Spring, S., Alm, C., Vousden, D.A., Palmert, M.R., Lerch, J.P., 2013. Hippocampal volumes differ across the mouse estrous cycle, can change within 24 hours, and associate with cognitive strategies. NeuroImage 83, 593–598.

Sepulveda, M.R., Dresselaers, T., Vangheluwe, P., Everaerts, W., Himmelreich, U., Mata, A.M., Wuytack, F., 2012. Evaluation of manganese uptake and toxicity in mouse brain during continuous MnCl2 administration using osmotic pumps. Contrast Media Mol. Imaging 7, 426–434.

Shukakidze, A., Lazriev, I., Mitagvariya, N., 2003. Behavioral impairments in acute and chronic manganese poisoning in white rats. Neurosci. Behav. Physiol. 33, 263–267.

Sillitoe, R.V., Joyner, A.L., 2007. Morphology, molecular codes, and circuitry produce the three-dimensional complexity of the cerebellum. Annu. Rev. Cell Dev. Biol. 23, 549–577.

Sillitoe, R.V., Vogel, M.W., Joyner, A.L., 2010. Engrailed homeobox genes regulate establishment of the cerebellar afferent circuit map. J. Neurosci. 30, 10015–10024.

Silva, A.C., Lee, J.H., Aoki, I., Koretsky, A.P., 2004. Manganese-enhanced magnetic resonance imaging (MEMRI): methodological and practical considerations. NMR Biomed. 17, 532–543.

Silverman, J.L., Yang, M., Lord, C., Crawley, J.N., 2010. Behavioural phenotyping assays for mouse models of autism. Nat. Rev. Neurosci. 11, 490–502.

Sled, J.G., Zijdenbos, A.P., Evans, A.C., 1998. A nonparametric method for automatic correction of intensity nonuniformity in MRI data. IEEE Trans. Med. Imaging 17, 87–97.

Spring, S., Lerch, J.P., Henkelman, R.M., 2007. Sexual dimorphism revealed in the structure of the mouse brain using three-dimensional magnetic resonance imaging. NeuroImage 35, 1424–1433.

Stoodley, C.J., Valera, E.M., Schmahmann, J.D., 2012. Functional topography of the cerebellum for motor and cognitive tasks: an fMRI study. NeuroImage 59, 1560–1570.

Sudarov, A., Joyner, A.L., 2007. Cerebellum morphogenesis: the foliation pattern is orchestrated by multi-cellular anchoring centers. Neural Dev. 2, 26.

Szulc, K.U., Nieman, B.J., Houston, E.J., Bartelle, B.B., Lerch, J.P., Joyner, A.L., Turnbull, D.H., 2013. MRI analysis of cerebellar and vestibular developmental phenotypes in Gbx2 conditional knockout mice. Magn. Reson. Med. 70, 1707–1717.

Szyf, M., Weaver, I.C., Champagne, F.A., Diorio, J., Meaney, M.J., 2005. Maternal programming of steroid receptor expression and phenotype through DNA methylation in the rat. Front. Neuroendocrinol. 26, 139–162.

Turnbull, D.H., Mori, S., 2007. MRI in mouse developmental biology. NMR Biomed. 20, 265–274.

van Eede, M.C., Scholz, J., Chakravarty, M.M., Henkelman, R.M., Lerch, J.P., 2013. Mapping registration sensitivity in MR mouse brain images. NeuroImage 82, 226–236.

Wadghiri, Y.Z., Blind, J.A., Duan, X., Moreno, C., Yu, X., Joyner, A.L., Turnbull, D.H., 2004. Manganese-enhanced magnetic resonance imaging (MEMRI) of mouse brain development. NMR Biomed. 17, 613–619.

Watanabe, T., Frahm, J., Michaelis, T., 2010. Myelin mapping in the living mouse brain using manganese-enhanced magnetization transfer MRI. NeuroImage 49, 1200–1204.

Yu, X., Wadghiri, Y.Z., Sanes, D.H., Turnbull, D.H., 2005. In vivo auditory brain mapping in mice with Mn-enhanced MRI. Nat. Neurosci. 8, 961–968.

Yu, X., Nieman, B.J., Sudarov, A., Szulc, K.U., Abdollahian, D.J., Bhatia, N., Lalwani, A.K., Joyner, A.L., Turnbull, D.H., 2011. Morphological and functional midbrain phenotypes in Fibroblast Growth Factor 17 mutant mice detected by Mn-enhanced MRI. NeuroImage 56, 1251–1258.